PHYSICAL REVIEW B **81**, 205427 (2010)

Monte Carlo simulations of argon adsorption in nanoscopic linear channels

Marco Da Re,[1] Sonja Grubišić,[1,2,3] and Francesco Ancilotto[1,2]
[1]*Dipartimento di Fisica "G. Galilei," Università di Padova, via Marzolo 8, I-35131 Padova, Italy*
[2]*CNR-IOM-Democritos, I-34014 Trieste, Italy*
[3]*Center for Chemistry, Institute of Chemistry, Technology and Metallurgy, University of Belgrade, Njegoševa 12, P.O. Box 815, 11001 Belgrade, Serbia*

(Received 18 February 2010; revised manuscript received 15 April 2010; published 19 May 2010)

We have studied, using grand canonical Monte Carlo simulations, the adsorption of Ar at 85 and 128 K inside nanoscopic open channels of different cross-section shapes on an Al surface. We studied, in particular, the filling phenomenology in linear channels whose cross sections are shaped like a cusp, wedge, parabola, and square well. The influence of the channel geometry on the adsorption behavior is analyzed by computing the adsorption isotherms. Different growth regimes are found as the adsorption proceeds, which are compared with existing model calculations and experimental data. Our simulations show, in particular, the occurrence, in square-well channels, of a nanoscale version of the so-called "Moses transition," in agreement with the predictions of model calculations and with recent experimental results.

DOI: 10.1103/PhysRevB.81.205427 PACS number(s): 68.08.Bc, 02.50.Ey, 05.40.−a, 82.20.Uv

I. INTRODUCTION

The synthesis, characterization, and processing of nanostructured materials are part of an emerging and rapidly growing field. Research and development in this field emphasizes scientific advances in the generation of materials with controlled microstructural characteristics. Techniques for fabricating on submicron length scales span a wide range, from sophisticated lithographic methods to more recent materials and chemical advances that rely on self-organization. Several approaches for fabricating patterns below 100 nm have been proposed, including nanoimprint lithography, near-field optical lithography, direct patterning on a nanometer scale with scanning-probe microscopes, self-assembly of monolayers, pattern formation based on phase separation of polymers, etc. The modern technology progress in the fabrication of micropatterned materials allows, in particular, to study a very important subject, i.e., the adsorption of fluids on tailored surfaces, thus allowing to directly test theoretical predictions in this field. As an example, the wetting behavior of liquid films in linear channels shows a rich variety of novel phase transitions that are sensitive to the shape of the confining geometry,[1–4] some of which were likely observed in adsorption experiments.[5–7] As a second example, it was found that complete wetting of substrates patterned by periodic arrays of rectangular wells and quadratic lattices of cylindrical pits, both of same depths, exhibits an example of geometrical covariance.[3] It was also predicted that capillary condensation in a capped slit is a continuous interfacial critical phenomenon, intimately related to several other surface phase transitions.[8] Recently, density-functional calculations of adsorption of liquid helium on alkali metal surfaces (which are the prototypes of weakly adsorbing substrates) structured with a lattice of parabolic nanocavities have revealed a rich adsorption phase diagram caused by the presence of the cavities, which acts as weak condensing sites, and the flat regions surrounding them, which favor the formation of thin films.[9] The present work summarizes the results of a theoretical study, based on classical Monte Carlo (MC) simulations, of the growth of liquid Ar films adsorbed within an array of nanoscopic open channels of different cross-section shapes on an Aluminum surface. Our aim is to help clarifying the role that surface geometry plays in fluid adsorption on nanostructured substrates, and also to compare our findings with the theoretical results based on the Rascón and Parry's model of Refs. 1 and 10 and with experimental measurements of fluid adsorption within channels of microscopic sizes reported in Refs. 3 and 7. We follow here a complementary, atomic-scale view of adsorption whereas the model discussed in Rascón and Parry paper has been formulated for a macroscopic system and is not intended to give a microscopic description of these phenomena, the atomic structure of the adsorbed film being completely neglected.

Our paper is arranged as follows. In Sec. II the theoretical model developed by Rascón and Parry is briefly summarized. Secs. III A and III B describe the grand canonical Monte Carlo (GCMC) simulation technique used in our work and the method used to generate reliable adsorption potentials for the nanoscopic channels. The central results of our work are presented and discussed in Sec. IV while Sec. V contains some concluding remarks.

II. RASCÓN-PARRY MODEL

In this work we will refer to the model discussed by Rascón and Parry in Refs. 1 and 10, and for this reason we briefly summarize here its main conclusions. The authors have shown, on the basis of a purely geometrical model, how the adsorption properties of a substrate are affected by the geometrical shape of the adsorbing surface. In particular, they discussed the adsorption of a fluid within linear channels (of infinite length) with cross section described by the function

$$z(x) = B|x - L_x/2|^{\gamma}, \tag{1}$$

where B is a shape factor, $x \in [0, L_x]$, y is the coordinate parallel to the channels and L_x is the width of the channel.

TABLE I. Exponent w in Eq. (2) predicted by the Rascón-Parry model, for a channels whose cross section is given by Eq. (1).

	w Preasymptotic regime	w Asymptotic regime
$\gamma=0$ (flat surface)		$-1/3$
$\gamma\leq 1/2$	$-\gamma/3$	$-1/3$
$1/2<\gamma\leq 1$	$-\gamma/3$	$-\gamma/(2-\gamma)$
$1<\gamma\leq 2$	$-1/3$	$-\gamma$
$\gamma>2$		$-\gamma$

These substrate shapes range smoothly from a planar wall for $\gamma=0$ to a capillary slit for $\gamma\rightarrow+\infty$.

The model has been formulated for a macroscopic system and is not intended to give a microscopic description of the adsorption phenomena: the atomic structure of the adsorbed film is completely neglected, as in the derivation of the Frenkel-Halsey-Hill relation[11,12] which describes the asymptotic film growth on a flat surface. In the case of van der Waals (VdW) forces between the adatom and the substrate, this relation states that in the asymptotic limit ($\Delta\mu\rightarrow 0^+$), the coverage Γ is proportional to $(\Delta\mu)^{-1/3}$, where $\Delta\mu$ represents the deviation of the chemical potential of the bulk vapor in equilibrium with the film from its saturation value μ_0. In spite of the macroscopic character of the model, we summarize here its main results because, as we will show in the following, similarities with the results of our microscopic calculations can indeed be found. According to the authors, the substrate is always coated with a liquid layer (*primary layer*) of thickness ℓ_π, which is the thickness of a film adsorbed on a flat surface made of the same material, at the same temperature and pressure. The adsorbed fluid is composed of this primary layer and, possibly, of extra liquid. The term *meniscus* refers to the surface of this extra liquid as it smoothly connects to the surface of the primary layer.

The model predicts that the midpoint thickness ℓ_0 diverges continuously (on approaching coexistence) falling within different regimes depending on the value of γ. For $0\leq\gamma\leq 2$, the asymptotic behavior is preceded by a preasymptotic one, both of which are characterized by a relation

$$\ell_0 \propto (\Delta\mu)^w. \tag{2}$$

The exponents w are listed in Table I.

When $0\leq\gamma\leq 2$, during the whole adsorption process a convex, cylindrical meniscus is always formed. In the case $\gamma>2$, at a particular value of $\Delta\mu$, *two* menisci appear, symmetrically placed with respect to the channel center. Approaching coexistence, these menisci increase in size until they merge into a single one (Moses transition) while the asymptotic behavior is eventually determined by the exponent $w=-\gamma$.

III. COMPUTATIONAL DETAILS

A. Monte Carlo simulations

MC techniques have been developed in order to probe the statistically important regions in the configuration space of a physical system. These techniques generate a sample of microstates which is *a priori* weighted according to the probability distribution of the selected statistical ensemble[13,14] so that the macroscopic quantities can be obtained by simple arithmetic means.

In our simulations, we have applied the original algorithm, as proposed by Metropolis *et al.*,[15] in the framework of the GCMC ensemble, i.e., at fixed chemical potential μ, volume V, and temperature T. This is the most natural choice to describe adsorption phenomena because the adsorbed liquid film and the coexisting vapor represent two systems in equilibrium which can continuously exchange energy and particles.

Given a starting configuration (coordinates of the Ar atoms), every iteration of the algorithm consists of a small random change in the configuration (see the following). If the new configuration is more probable than the old one, the move is accepted; otherwise, it is accepted with a probability equal to the probability ratio between the new and the old configurations. In the present case, three types of trial moves are attempted: (a) displacement of an Ar atom, with a transition probability equal to $\exp(-\frac{\Delta E}{kT})$; (b) insertion of an Ar atom in the simulation box (supercell), with a transition probability of $\frac{V}{\Lambda^3(N+1)}\exp[-\frac{(-\mu+\Delta E)}{kT}]$; and (c) removal of an Ar atom, with a probability equal to $\frac{\Lambda^3 N}{V}\exp[-\frac{(\mu+\Delta E)}{kT}]$. In these expressions ΔE is the potential energy difference between the new and the old microstate, N is the number of Ar atoms in the simulation cell, k is the Boltzmann constant, and Λ is the De Broglie wavelength of the atom. Once the equilibrium is reached, the system is therefore sampled at regular intervals. We have chosen the number of moves in order to sample the system every 5/10 times the number of atoms and to collect 6000/10 000 samples altogether: with this choice, consecutive samples are essentially uncorrelated while the CPU time required for the simulation remains affordable (see Refs. 13 and 16)

The fraction of trials for atom displacement, insertion, and removal amounted to 50%, 25%, and 25%, respectively, and the maximum allowed displacement was adjusted in order that the displacement acceptance ratio were 50%. We have computed the isotherms for both adsorption and desorption processes at two different temperatures, $T=85$ K (i.e., just above the bulk triple-point temperature for Ar, $T_t=83.8$ K) and $T=128$ K (i.e., well below the Ar critical point, $T_c=150.9$ K). These isotherms are presented as relations between the coverage Γ and the chemical potential μ. The latter is related to the vapor pressure p by[17]

$$\frac{\mu-\mu_{id}}{k_B T}=-\ln(1+Q)+2Q, \tag{3}$$

where $Q=[(4Bp/T+1)^{1/2}-1]/2$, μ_{id} is the chemical potential of the ideal gas and B is the second virial coefficient of the Ar gas.

The coverage is defined here as the number of adsorbed atoms per unit of surface area

$$\Gamma=\frac{1}{S}\int d\mathbf{r}\mathrm{Max}\{0,[\rho(\mathbf{r})-\rho_v]\}, \tag{4}$$

where S is the x-y surface of the unit cell, perpendicular to the symmetry axis, and ρ_v is the vapor density at coexistence with the Ar fluid at the given temperature obtained from the bulk equation of state. The experimental counterpart of the above quantity, is the amount of fluid adsorbed on the substrate in torsional/quartz microbalance experiments.

In all cases, the substrate is located at the bottom of the supercell whereas on the top of it a purely repulsive potential wall is used to keep the atoms inside the supercell during the simulations. A vacuum region is added between the substrate and the repulsive wall to allow for the formation of a sufficiently thick vapor buffer in equilibrium with the adsorbed liquid. Periodic boundary conditions are imposed during the simulations, leading to a periodic array of linear channels of a given shape. This is the usual situation encountered in experiments,[7] i.e., substrates patterned with regular arrays of nano/microindentations rather than single, isolated channels.

At a given value of T and V, for each shape of the cross section of the channel (see below), we have started the calculations with μ well below the coexistence value (corresponding to a very small number of Ar atoms in the supercell, $N \cong 20$) and gradually increased its value until the channels were completely filled. Complete filling occurs just below the coexistence value because of the finite height of the channel and of a phenomenon (see the following) similar to capillary condensation.[18]

The coordinate system was chosen in such a way that the channels are parallel to the y axis. We have chosen four different shapes of the cross section, which are defined by the following functions:

$$z = B_{1/2}|x - L_x/2|^{1/2}(\text{cusp})(B_{1/2} = 13.2 \ \text{Å}^{1/2})$$

$$z = B_1|x - L_x/2|(\text{wedge})(B_1 = 1.8 \ \text{Å}^0)$$

$$z = B_2|x - L_x/2|^2(\text{parabola})(B_2 = 3.5 \times 10^{-2} \ \text{Å}^{-1})$$

$$z = B_6|x - L_x/2|^6(\text{6-channel})(B_6 = 4.6 \times 10^{-9} \ \text{Å}^{-5})$$

The dimensions of the supercell were: $L_x = 105.03$ Å; $L_y = 45.76$ Å; and $L_z = 183.80$ Å. We have fixed the B constants so that $z(0) = z(L_x) = 95.48$ Å. In this way, the supercell contained up to about 10 000 atoms. The last case (6 channel) is taken here as representative of a channel whose cross section is close to a square-well profile.

The interaction between Ar atoms is calculated by using a Lenard-Jones pair potential (which is known to give results for the bulk phase in rather good agreement with the experimental phase diagram, at least not too close to the critical point[19])

$$V(\mathbf{r}) = 4\epsilon\left[\left(\frac{\sigma}{r}\right)^{12} - \left(\frac{\sigma}{r}\right)^{6}\right] \tag{5}$$

with $\epsilon = 119.8$ K and $\sigma = 3.41$ Å.

There is a variety of metal surfaces that are examples of strongly attractive substrates for inert gas adatoms. Aluminum has been chosen here, both because it is often used as a substrate for experimental studies of fluid adsorption, and also because the interaction potential between an Ar atom and an Al planar surface has been recently calculated[20] using a novel *ab initio* method which allows us to properly account for the adatom-surface Van der Waals interactions.[21]

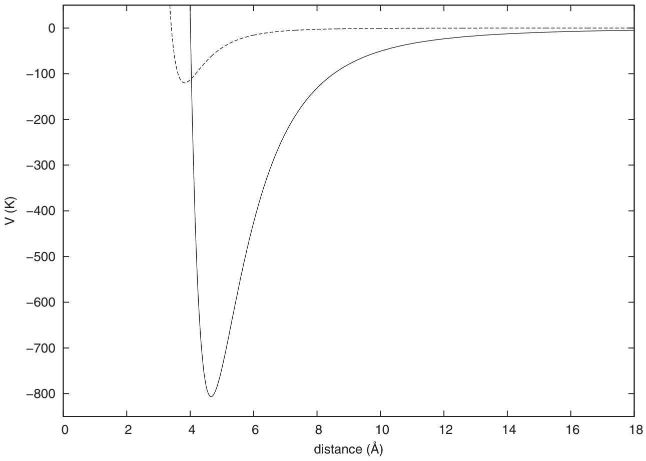

FIG. 1. Comparison between the Ar-Ar potential (dashed line) and the Ar-Al surface potential (solid line).

We have derived, from the results reported in Ref. 20, an effective potential which describes the overall adsorption properties of a model, planar Al surface; it has recently been used[22] to study the adsorption properties of Ar on nanoporous Al substrates. In particular, we averaged, for a given distance from the surface, the Ar-surface potential as calculated in Ref. 20 over different adsorption sites, in order to obtain a z-dependent only function V_s (z being the Ar-surface distance). The resulting potential has a minimum value $V_s(z_0) = -72.27$ meV, at a distance from the surface $z_0 = 4.67$ Å. The inclusion of VdW effects, as done in Ref. 20, is expected to give reliable values for the binding energy and equilibrium distance of the Ar atom; unfortunately, a proper calculation of the long-range tail of the adatom-surface potential, using the same *ab initio* approach, is difficult, due to the very big size required for the supercell. For this reason we modeled the long-range VdW tail of the atom-surface potential, $\sim C_3/z^3$, using the value of C_3 computed in Ref. 23 by direct summation of the frequency-dependent polarizabilities. The potential $V_s(z)$, describing the interaction between the Ar atom and an Al planar substrate was obtained by fitting the averaged *ab initio* results with a simple functional form written in terms of a short-range repulsion and long-range van der Waals attractions, namely,

$$V_s(z) = \frac{A}{z^9} - \frac{C_5}{z^5} - \frac{C_3}{z^3}. \tag{6}$$

The two parameters A and C_5 are adjusted in such a way to reproduce both the minimum depth V_0 and the position z_0 in the averaged potential obtained from the *ab initio* calculations. The value of the parameters are as follows: $A = 8.25497 \times 10^4$ eV Å^9; $C_3 = 1.490$ eV Å^3; and $C_5 = 2.95683 \times 10^2$ eV Å^5.

The Ar-Al surface average potential is shown in Fig. 1 as a function of the Ar surface distance. For comparison, the much weaker Ar-Ar interatomic potential is also shown.

B. Adsorption potential for a nonplanar substrate

Although the adsorption of classical and quantum fluids on *nonplanar* substrates is an important field of research, a

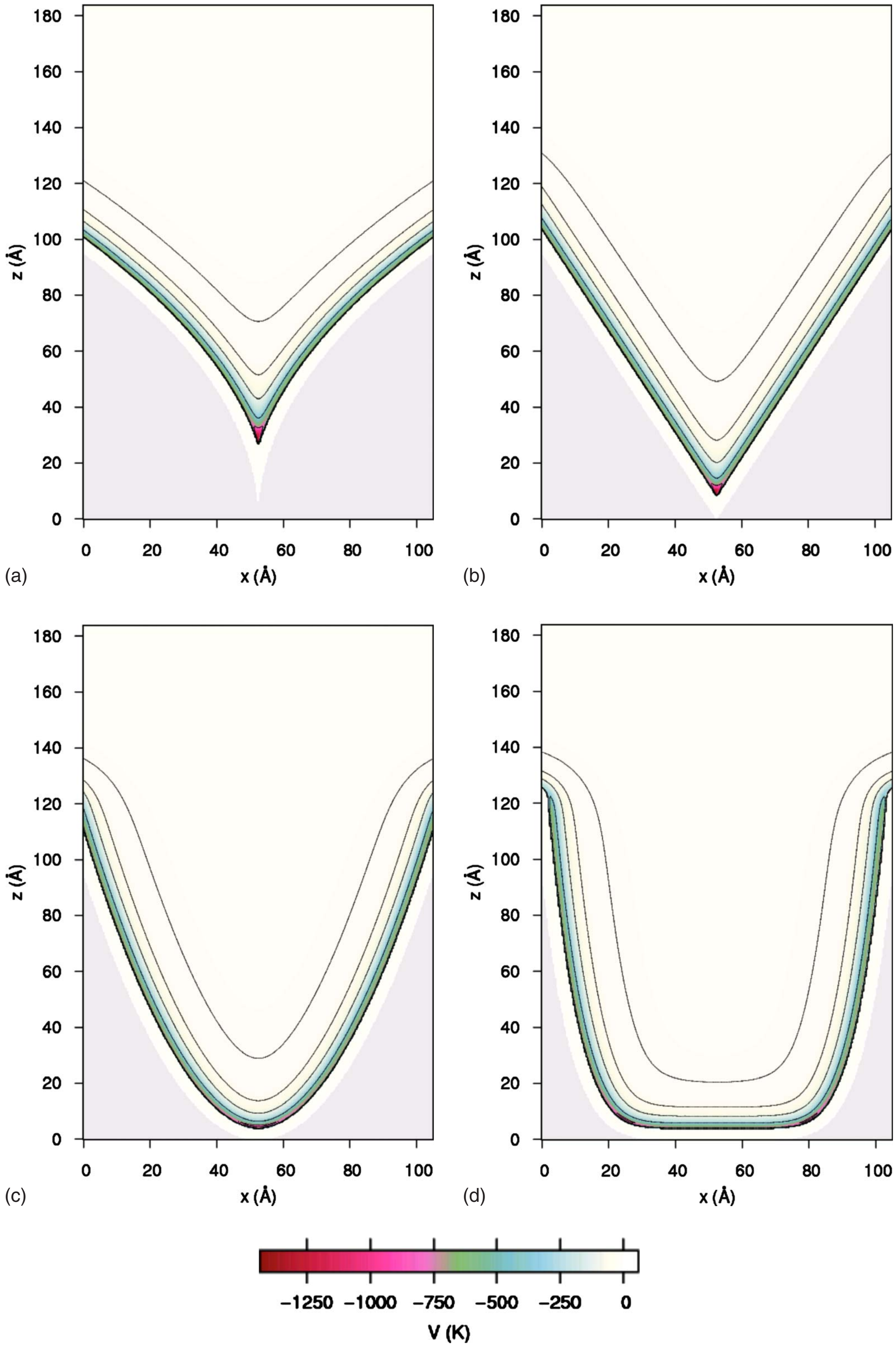

FIG. 2. (Color online) Maps of the interaction potential between an Ar atom and a linear channel shaped as a (a) cusp; (b) wedge; (c) parabola; and (d) 6-channel. The isopotential lines correspond to: −3, −25, −100, −400, and −850 K.

reliable form for the interaction experienced by an adatom in such a situation is not usually known even if accurate potentials are available for describing the interaction of the adatom with a planar surface of the same material.

To properly describe the interaction of Ar atoms with the patterned Al substrates described in the previous section, we adopt here a recently developed technique, namely, the *elementary source method*,[24] which allows to determine the

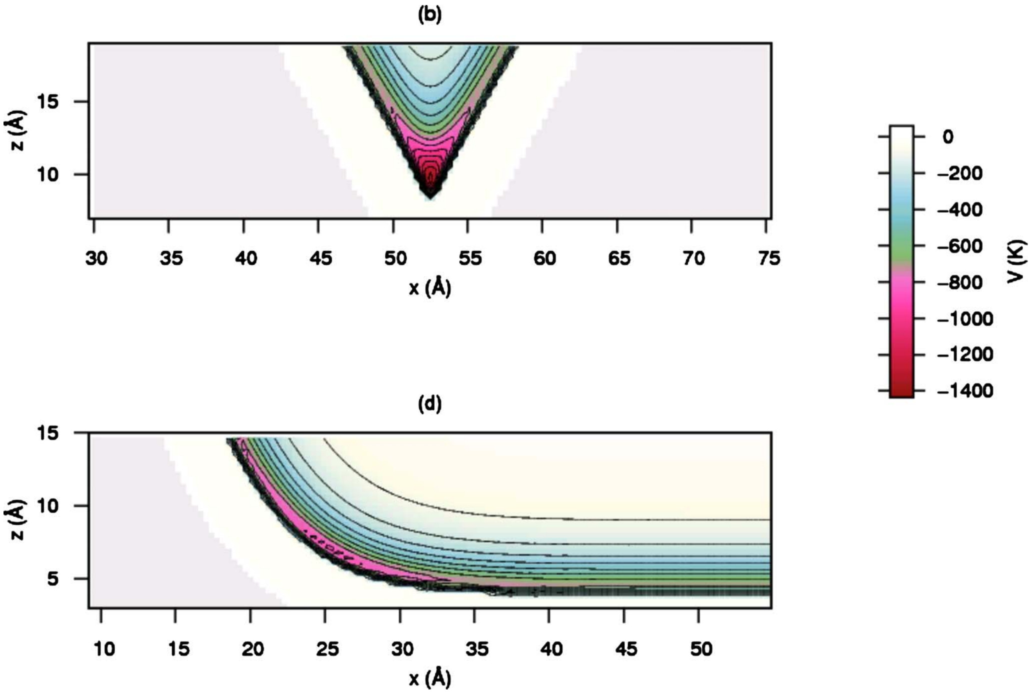

FIG. 3. (Color online) Details of the interaction potentials between an Ar atom and a (b) wedge; (d) 6-channel, close to the minimum of the potential. The isopotential lines correspond to values from −1470 to −70 K, at intervals of 100 K.

adsorption potential for nonplanar geometries, provided the potential for a planar surface of the same material is known. This method derives the elementary contribution of a differential source of the substrate by assuming a continuous distribution of matter. Once this elementary contribution is obtained, it can afterward be integrated, weighted with a density that corresponds to the chosen surface topology. The method is numerically fast and robust, and gives rise to potential landscapes that account adequately for the topology of the surface. If the solid is defined by the inequality $\psi(\mathbf{r})>0$, the potential energy $V_{ext}(\mathbf{r})$ for an atom at $\mathbf{r}$ is computed as

$$V_{ext}(\mathbf{r}) = \int \frac{d\mathbf{r}'}{2\pi} H[\psi(\mathbf{r}')] \frac{V_s''(|\mathbf{r}-\mathbf{r}'|)}{|\mathbf{r}-\mathbf{r}'|}, \tag{7}$$

where H is the Heaviside step function and V_s is the interaction potential between the adatom and the planar surface. In our case, $V_{ext}(\mathbf{r})$ has been computed in the unit supercell using in the above integral the contribution of the first neighboring cells as well, to account for the effect of the periodicity of the channel arrangement.

TABLE II. Positions and values of the minima of the interaction potentials between an Ar atom and the four Al substrates.

	z_{min} (Å)	V_{min} (K)
Flat surface	4.67	−806.68
Cusp	29.26	−1388.99
Wedge	9.75	−1425.48
Parabola	4.50	−908.64
6-channel	6.75	−892.74

The landscapes for the adsorption potentials calculated using Eq. (7) are shown in Fig. 2 and 3. As can be seen from the figures, absolute minima in the potential appear close to the apex of the channels section, and they can be much deeper than the local minima close to the planar part of the channel walls. Moreover, the minima for the cusp and wedge are deeper than the ones for the parabola and the 6-channel. The values and positions of the minima of the four adsorption potentials (and, for reference, of the Ar-Al flat surface potential) are listed in Table II: for the 6-channel, there are *two* symmetric minima with respect to the central *yz* plane

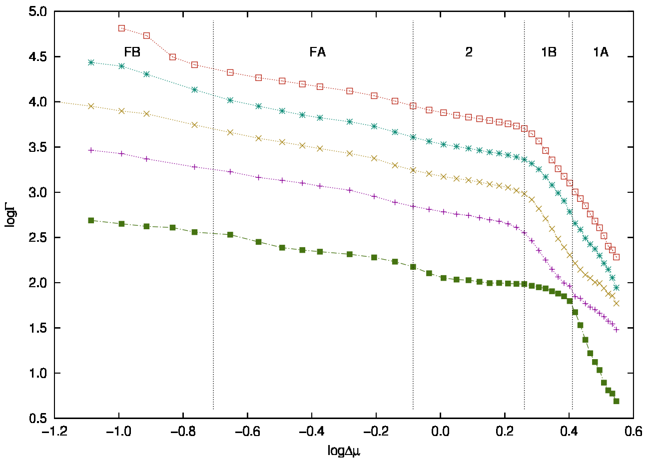

FIG. 4. (Color online) Adsorption isotherms at $T=85$ K of Argon on the Al planar surface (filled squares), cusp (plusses), wedge (crosses), parabola (stars), and 6-channel (open squares).

TABLE III. Exponents w of Eq. (8) calculated along different portions of the isotherms at $T=85$ K.

	$w_{1\text{A}}$	$w_{1\text{B}}$	w_2	w_{FA}	w_{FB}
Cusp	−2.71	−4.74	−0.64	−0.48	−0.57
Wedge	−2.90	−5.41	−0.60	−0.61	−0.68
Parabola	−5.12	−4.5	−0.58	−0.64	−1.02
6-channel	−5.56	−5.03	−0.60	−0.56	−1.92
Flat surface					−0.34

(see the bottom panel of Fig. 3). As shown in the following Section, these minima have a remarkable effect in the early stages of Ar adsorption in this type of channels, giving rise to two menisci which, as the coverage grows, eventually merge into a single one.

IV. RESULTS AND DISCUSSIONS

We have calculated, for each type of channel, the coverage Γ as a function of the deviation $\Delta\mu$ of the chemical potential of bulk vapor in equilibrium with the film from its saturation value. In the following, the values of the chemical potentials will be expressed in reduced units, where the energy unit is equal to the Ar-Ar potential well depth, $\epsilon=119.8$ K. The adsorption isotherms $\Gamma(\Delta\mu)$ at $T=85$ K and $T=128$ K, for each channel shape, are shown on a log-log scale in Figs. 4 and 5. We have verified that the desorption isotherms are identical to the adsorption ones, i.e., there is no hysteresis for any channel shape.

We identified different intervals of $\log(\Delta\mu)$ values where the corresponding values of $\log(\Gamma)$ follow roughly a linear behavior but with different slopes. The labels in the Figs. 4 and 5, and the vertical dashed lines which separate the corresponding regions, are only indicative: when discussing the results, we refer exclusively to the intervals in which the points follow a clear linear behavior so that a linear interpolation can be reliably used there.

This linear behavior signals a power-law dependence of the coverage versus chemical potential; every interval corresponds to a growth regime of the adsorbed film in which

$$\Gamma \propto (\Delta\mu)^w. \tag{8}$$

From now on, these growth regimes, and the corresponding intervals within the isotherm, will be identified (in order of increasing coverage Γ) by the labels 1A, 1B, 2, FA, and FB.

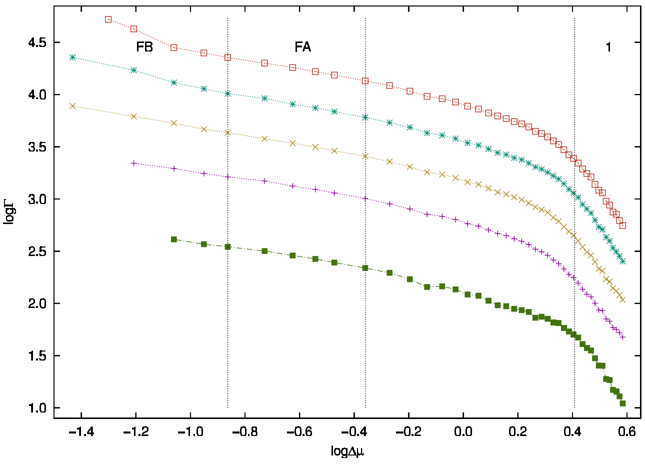

FIG. 5. (Color online) Adsorption isotherms at $T=128$ K of Argon on aluminum flat surface (filled squares), cusps (plusses), wedges (crosses), parabolae (stars), and 6 channels (open squares).

Each of these regimes corresponds, approximately, to the same range of $\Delta\mu$. By looking at the actual density profiles in the various regimes, we note that: (1) within 1A and 1B, the first monolayer of adsorbate starts to grow. In particular, in the low-coverage 1A branch there is only a "seed" present, composed of atoms adsorbed within the most attractive region(s), where the adatom-substrate potential attains its lowest values. Along the 1B branch of the isotherms the first monolayer appears, slowly invading the nearby portions of the channel walls. (2) Between 1B and 2, the first monolayer is completed and the seed of the second layer appears; (3) during 2, the second monolayer grows. In cusp and wedge channels one can see the seeds of the third monolayer as well whereas on parabolae and 6-channels these appear later; (4) between 2 and FA, the second monolayer completes; and (5) during FA and FB, the channel becomes filled.

In the $T=128$ K isotherms (Fig. 5), the calculated points follow approximatively a linear behavior only in the interval of $\Delta\mu$ corresponding to the growth of the first monolayer (labeled with 1: at this higher temperature, we cannot distinguish two separate regimes during this process, as it happens at the lower temperature) and in one (cusps and wedges) or two (parabolae and 6-channels) intervals corresponding to the final stage of the filling process (labeled with FA and FB, respectively).

The calculated exponents w, for the two values of T, are listed in Tables III and IV. The errors associated with the calculated exponents (which derives essentially from the interpolation procedure) are between 0.07 and 0.15 for the $w_{1\text{A}}$ and $w_{1\text{B}}$ exponents, whereas they are smaller (between 0.01

TABLE IV. Exponents w of Eq. (8) calculated along different portions of the isotherms at $T=128$ K.

	w_1	w_{FA}	w_{FB}
Cusp	−3.22	−0.37	
Wedge	−3.51	−0.44	
Parabola	−3.82	−0.50	−0.63
6-channel	−3.98	−0.44	−0.96
Flat surface			−0.34

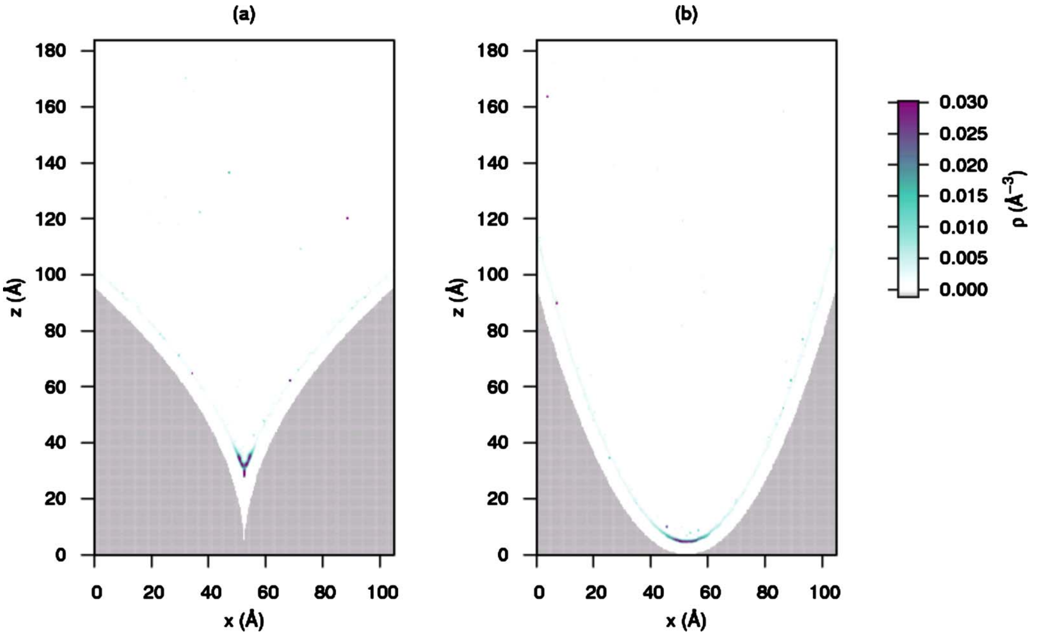

FIG. 6. (Color online) Density profiles of Argon adsorbed on aluminum (a) cusps and (b) parabolae at $\mu=-1509$ K ($\log \Delta\mu=0.494$, region 1A) and $T=85$ K.

and 0.03) for the other exponents. Only w_{FB} for the 6-channels is affected by a somewhat larger error bar, about 0.3.

The exponent $w_{1\mathrm{A}}$ associated with the growth of the first monolayer at $T=85$ K appears to strongly depend on the shape of the channel cross section. In particular, the values of $w_{1\mathrm{A}}$ for cusps and wedges are very close to each other, and so are the values for parabolae and 6-channels; the latter ones are comparable to the values found for $w_{1\mathrm{B}}$, which do not differ instead very much from one another.

The density profiles of Argon adsorbed on all the investigated structures at 85 K are shown in Figs. 6–9. As already noted, for very low coverages (1A phase), the adatoms arrange themselves where the adatom-substrate potential is most attractive. The potential wells of cusps and wedges are much deeper and more localized in space (Figs. 2 and 3 and Table II) than the wells of parabolae and 6-channels. Indeed, the seed of the first monolayer on parabolae [Fig. 6(a)] and 6-channels (for the latter shape, there are *two* separate seeds because the interaction potential has two symmetric minima)

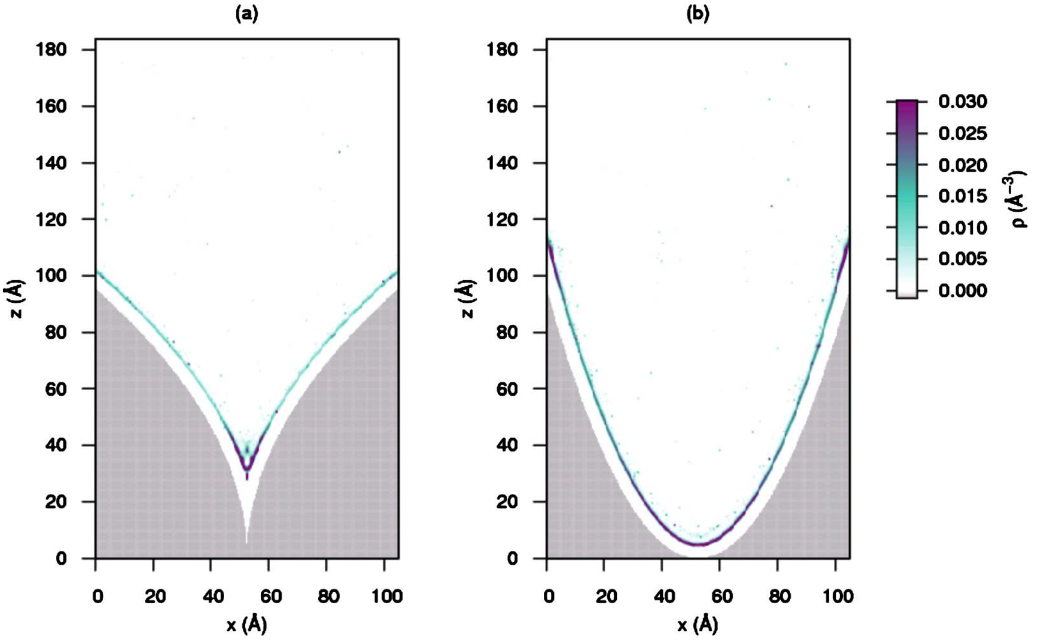

FIG. 7. (Color online) Density profiles of Argon adsorbed on aluminum (a) cusps and (b) parabolae at $\mu=-1390$ K ($\log \Delta\mu=0.327$, region 1B) and $T=85$ K.

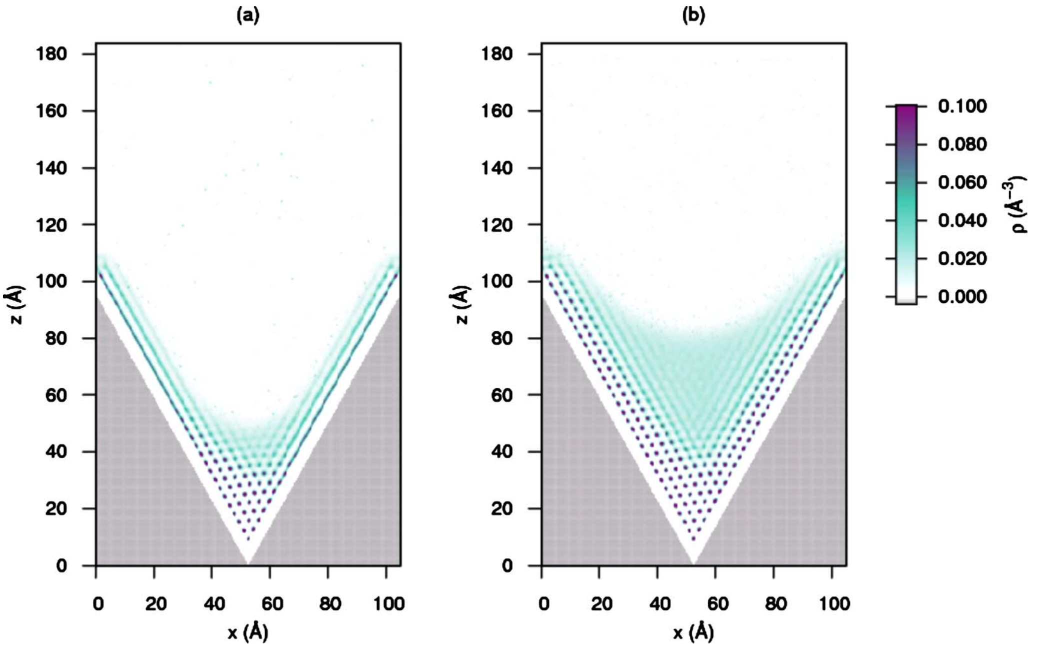

FIG. 8. (Color online) Density profiles of Argon adsorbed on aluminum wedges at $T=85$ K and (a) $\mu=-1168$ K ($\log \Delta\mu=-0.565$, region FA); (b) $\mu=-1148$ K ($\log \Delta\mu=-0.991$, region FB).

is somewhat spread out around the bottom of the channel profile whereas for cusps [Fig. 7(a)] and wedges, it is essentially made by a single row of atoms along the channel axis (similarly to the low-coverage phases of classical or quantum fluids adsorbed on the outer surface of bundles of carbon nanotubes[25,26]).

This explains the differences in the values of w_{1A} exponent and explains also why the values for parabolae and 6-channels are comparable to the values of w_{1B}: the rest of the monolayer, which appears during the 1B phase, has an essentially two-dimensional structure on all the four substrates [Figs. 6(b) and 7(b)]. The values of w_2, which could be calculated only at $T=85$ K, are even closer to one another than the w_{1B}: the presence of the first monolayer, which screens the attraction of the surface, and the increased distance from the surface, result in a reduced dependence of these exponents on the substrate geometry.

In the low-coverage region of the $T=128$ K isotherms, we could find a power law regime only during the growth of the first monolayer, and with only one exponent instead of

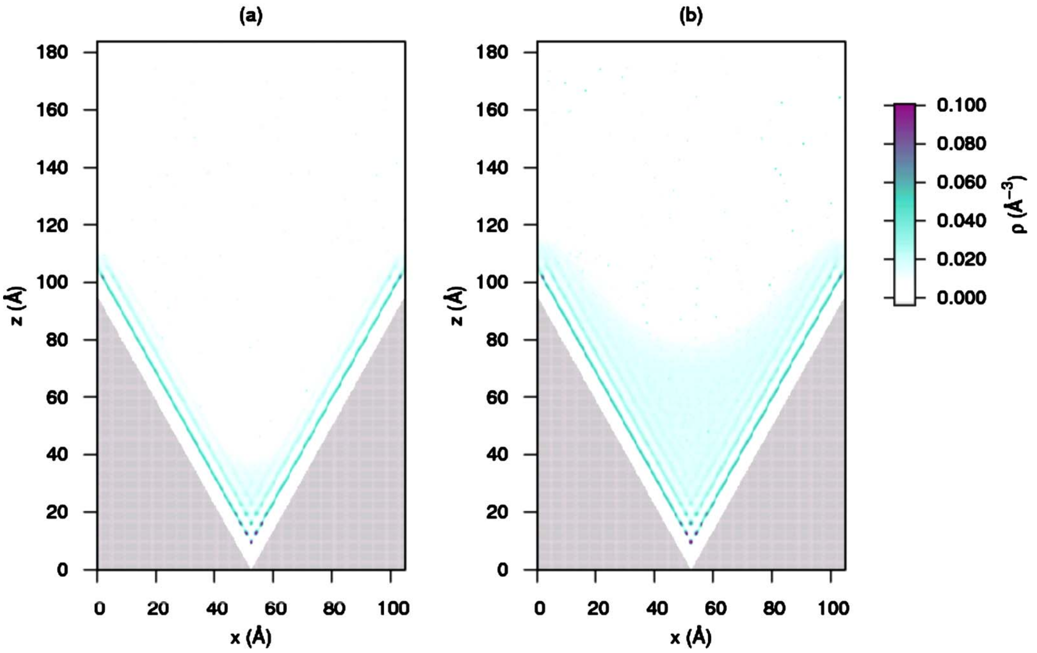

FIG. 9. (Color online) Density profiles of Argon adsorbed on aluminum wedges at $T=128$ K and (a) $\mu=-1498$ K ($\log \Delta\mu=-0.472$, region F); (b) $\mu=-1465$ K ($\log \Delta\mu=-1.208$, region F).

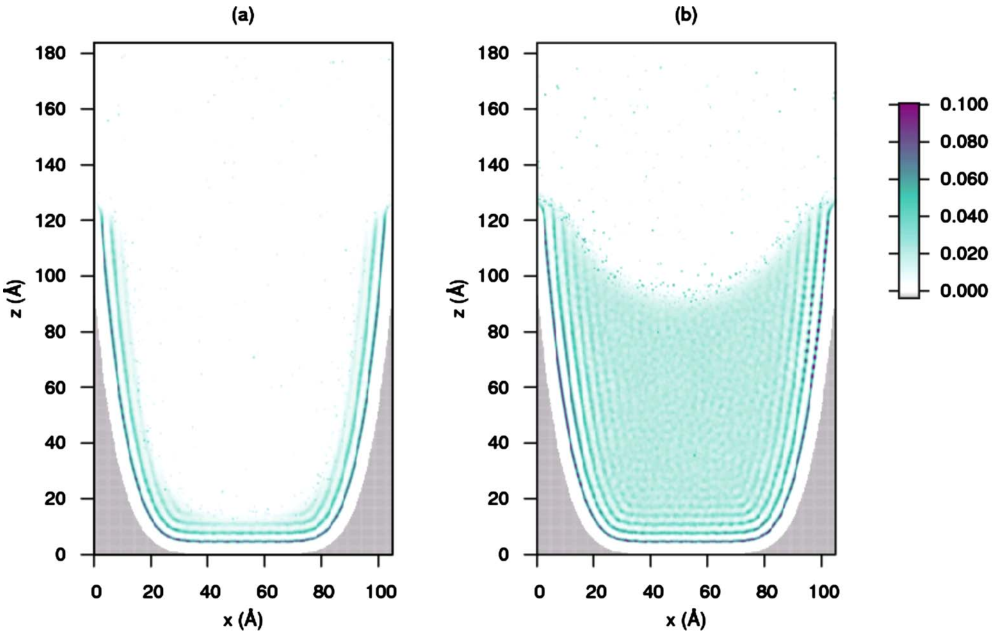

FIG. 10. (Color online) Density profiles of Argon adsorbed on aluminum 6-channels at $T=85$ K and (a) $\mu=-1174$ K ($\log \Delta\mu=-0.492$, region FA); (b) $\mu=-1148$ K ($\log \Delta\mu=-0.991$, region FB).

two. The exponent w_1 still depends on the geometry of the channel but to a smaller extent. The exponents w_{FA} and w_{FB} characterize the final stage of the adsorption isotherm, i.e., the filling of the channels: again, their value is affected by the geometry of the substrate. In particular, the exponent w_{FB} appears to increase with the (absolute) value of the γ exponent characterizing the channel section shape [see Eq. (1)].

Note that, similarly to what is assumed in the Rascon-Parry's model, the density plots for higher coverages show indeed the coexistence of a "thin film," uniformly covering the channel inner walls, with a convex, approximately cylindrical meniscus [see, for instance, Figs. 8–10].

Similarly to what in Ref. 1 is predicted to occur when the γ exponent in Eq. (1) is greater than 2, we find indeed evidence of a "Moses transition" on the nanoscale. By looking at the density profile in the "filling" regions FA and FB in, respectively, wedges and 6-channels, one can see that while in wedges there is only one meniscus for all coverages (and the same occurs on cusps and parabolae), in 6-channels there are clearly two menisci at lower coverages symmetrically placed with respect to the channel center (see Fig. 10, left panel) while at higher coverages they merge into a single, centered meniscus (see Fig. 10, right panel). This is clearly a consequence of the peculiar landscape of the adsorption potential for the 6-channels, which shows two symmetric minima (see Fig. 2), unlike the ones associated with cusps, wedges, and parabolae which have one minimum located at the channel apex. By examining the sequence of the density profiles, both at $T=85$ K and at $T=128$ K, we conclude that the merging of the two menisci in the Moses transition marks the separation between FA and FB regimes.

In order to better compare our results with the geometric model of Ref. 1, which is formulated in terms of the midpoint thickness ℓ_0 of the adsorbed film, rather than of the total coverage Γ, we have also computed the thickness ℓ_0 of the adsorbed Ar film from the density profiles $\rho(z)$ at the center of the channel. This is explicitly done by computing the Gibbs dividing surface position for each value of $\Delta\mu$. We show in Fig. 11 our results in a log-log plot. The values of l_0 are expressed in reduced units, in terms of the Ar-Ar Lenard-Jones parameter $\sigma=3.41$ Å. The range shown for l_0 corresponds to the "filling" regime ("asymptotic" regime in the Rascon-Parry's model), characterized by the sudden rise of the meniscus which follows a "preasymptotic" regime, characterized instead by the planar-surfacelike growth of the "thin-film" phase on the channel walls. The latter should correspond to values of $\Delta\mu$ in Fig. 11 greater than ~ -1. We cannot accurately describe this regime with our calculated l_0

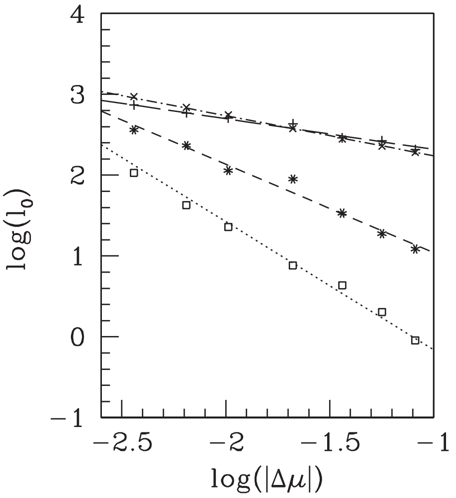

FIG. 11. Calculated midpoint thickness of Ar fluid, at $T=128$ K, adsorbed in cusps (plusses), wedges (crosses), parabolae (stars), and 6-channels (open squares). The best-fit interpolating lines are also shown.

TABLE V. "Asymptotic" growth exponents w in Eq. (2). In parenthesis we report the values calculated at $T=85$ K.

	w (Rascon-Parry model)	w (this work, $T=128$ K)
Cusp	−0.33	−0.38 (−0.47)
Wedge	−1.00	−0.50 (−0.63)
Parabola	−2.00	−1.09 (−0.98)
6-channel	−6.00	−1.58 (−0.82)

because the thin-film phase is made in our case, as it is clearly visible in the density plots, by just one or two solid-like atomic monolayers. A definition of the "thickness" variation in such films as a function of the chemical potential is problematic, also because the inhomogeneities in the adsorption potentials near the channel walls result in strong inhomogeneities of the fluid density within the atomic monolayers.

It appears from Fig. 11 that different power laws are found to characterize the film growth on different types of channels, in qualitative agreements with the predictions of the Rascon-Parry's model. The calculated exponents w entering Eq. (2) are easily extracted from a linear fit to the points in Fig. 11. The resulting values are shown in Table V, together with those predicted by the Rascón-Parry model in the asymptotic (filling) regime.

Although following the predicted trend with the channel geometry, our values for w substantially differ from those predicted by the Rascón-Parry model. In fact, as already mentioned above, the comparison with this model can only be qualitative because of its essentially macroscopic nature, as opposed to the nanoscopic scales involved in our calculations. Finite-size effects are expected for fluid adsorption on substrates with geometrical structures on the nanometer scale and they are likely to give substantially smaller effective values of the growth exponents.[27,28]

For the same reason, we cannot quantitatively compare our exponents with the ones found by Bruschi *et al.*[7] in their experimental work. They studied Argon adsorption, at $T=85$ K, within Silicon and Zeonex linear open channels whose cross section can approximately be described by Eq. (1), with $\gamma=0.5$, 1, and 3.3. The substrates used in these experiments belong to the class of strong adsorbers, such as the Al substrate studied here; the dimensions of their channels, however, are in the range of microns rather than of nanometers as in our calculations. The authors found different regimes in the adsorption isotherms, characterized by well-defined geometry-dependent growth exponents, in basic agreement with the predictions of the Rascón and Parry model.

V. CONCLUSIONS

In this work we have studied the adsorption of Ar on Aluminum substrates nanostructured with parallel open channels. Grand canonical Monte Carlo simulations have been used to explore the effects of the substrate geometry and temperature on the adsorption process, by considering channels of various cross-section shape. A completely reversible behavior (i.e., no hysteresis) of the adsorption-desorption cycle is observed for all channels.

We have found different power-law growth regimes in the calculated isotherms. The dependence of the exponents on the substrate geometry has been studied in detail. We have compared our results with the predictions of the geometrical model formulated by Rascón and Parry in Ref. 1 and found some similarities. The comparison can only be qualitative because of the scale differences (the geometrical model was formulated for a macroscopic system) but these similarities give us the opportunity to transpose to some extent their model to the atomic scale. For the same reason, the comparison with the experimental results of Ref. 7 is also only qualitative due to the micron-sized channels used there.

In agreement with the theoretical predictions of Ref. 1 and the experimental findings of Ref. 7, we find a clear evidence, when the shape exponent γ is greater than 2, of a Moses transition on the nanoscale where two menisci, initially localized on the sides of the channel merge into a single, centered meniscus as the chemical potential is further increased.

ACKNOWLEDGMENTS

We thank G. Mistura for useful comments and discussions. We acknowledge financial support from the Padova University under Project No. CPDA077281-07.

---

[1] C. Rascón and A. O. Parry, Nature (London) **407**, 986 (2000).

[2] E. Cheng and M. W. Cole, Phys. Rev. B **41**, 9650 (1990); K. Rejmer, S. Dietrich, and M. Napiorkowski, Phys. Rev. E **60**, 4027 (1999); A. O. Parry, C. Rascon, and A. J. Wood, Phys. Rev. Lett. **85**, 345 (2000); A. O. Parry, A. J. Wood, E. Carlon, and A. Drzewinski, *ibid.* **87**, 196103 (2001); S. Gheorghiu and P. Pfeifer, *ibid.* **85**, 3894 (2000); M. Heni and H. Lowen, *ibid.* **85**, 3668 (2000).

[3] M. Tasinkevych and S. Dietrich, Phys. Rev. Lett. **97**, 106102 (2006).

[4] E. S. Hernández, F. Ancilotto, M. Barranco, R. Mayol, and M. Pi, Phys. Rev. B **73**, 245406 (2006).

[5] L. Bruschi, A. Carlin, and G. Mistura, Phys. Rev. Lett. **89**, 166101 (2002).

[6] L. Bruschi, A. Carlin, A. O. Parry, and G. Mistura, Phys. Rev. E **68**, 021606 (2003).

[7] L. Bruschi, G. Fois, G. Mistura, M. Tormen, V. Garbin, E. di Fabrizio, A. Gerardino, and M. Natali, J. Chem. Phys. **125**, 144709 (2006).

[8] A. O. Parry, C. Rascon, N. B. Wilding, and R. Evans, Phys. Rev. Lett. **98**, 226101 (2007).

[9] F. Ancilotto, M. Barranco, E. S. Hernandez, A. Hernando, and M. Pi, Phys. Rev. B **79**, 104514 (2009).

[10] C. Rascón and A. O. Parry, Fluid Phase Equilib. **185**, 147

(2001).

[11] G. D. Halsey, J. Chem. Phys. **16**, 931 (1948).

[12] T. L. Hill, J. Chem. Phys. **17**, 590 (1949).

[13] M. P. Allen and D. J. Tildesley, *Computer Simulation of Liquids* (Clarendon Press, Oxford, 1987).

[14] D. Frenkel and B. Smit, *Understanding Molecular Simulation* (Academic Press, New York, 2001).

[15] N. Metropolis, A. W. Rosenbluth, M. N. Rosenbluth, A. H. Teller, and E. Teller, J. Chem. Phys. **21**, 1087 (1953).

[16] M. E. J. Newman and G. T. Barkema, *Monte Carlo Methods in Statistical Physics* (Clarendon Press, Oxford, 1999).

[17] M. J. Bojan, G. Stan, S. Curtarolo, W. A. Steele, and M. W. Cole, Phys. Rev. E **59**, 864 (1999).

[18] H. K. Christenson, Phys. Rev. Lett. **73**, 1821 (1994).

[19] J. A. Anta, E. Lomba, and M. Lombardero, Phys. Rev. E **55**, 2707 (1997).

[20] P. L. Silvestrelli, K. Benyahia, S. Grubišić, F. Ancilotto, and F. Toigo, J. Chem. Phys. **130**, 074702 (2009).

[21] P. L. Silvestrelli, Phys. Rev. Lett. **100**, 053002 (2008).

[22] S. Grubišić, M. Da Re, A. Hernando, P. L. Silvestrelli, F. Toigo, and F. Ancilotto (unpublished).

[23] C. Schwartz and R. J. Le Roy, Surf. Sci. **166**, L141 (1986).

[24] A. Hernando, E. S. Hernandez, R. Mayol, and M. Pi, Phys. Rev. B **76**, 115429 (2007).

[25] J. V. Pearce, M. A. Adams, O. E. Vilches, M. R. Johnson, and H. R. Glyde, Phys. Rev. Lett. **95**, 185302 (2005).

[26] S. M. Gatica, M. M. Calbi, R. D. Diehl, and M. W. Cole, J. Low Temp. Phys. **152**, 89 (2008).

[27] O. Gang, K. J. Alvine, M. Fukuto, P. S. Pershan, C. T. Black, and B. M. Ocko, Phys. Rev. Lett. **95**, 217801 (2005).

[28] C. Rascón, Phys. Rev. Lett. **98**, 199801 (2007).